Corrosion Science 235 (2024) 112174

Contents lists available at ScienceDirect

Corrosion Science

journal homepage: www.elsevier.com/locate/corsci

Plasma sprayed duplex ytterbium disilicate/monosilicate EBCs and the transformation from ytterbia to ytterbium monosilicate during burner rig testing

Emine Bakan [a,*], Dapeng Zhou [a], Daniel E. Mack [a], Dietmar Koch [b], Robert Vaßen [a]

[a] Forschungszentrum Jülich GmbH, Institute of Energy and Climate Research, Materials Synthesis and Processing (IEK-1), Jülich 52425, Germany
[b] University of Augsburg, Institute of Materials Resource Management, Augsburg 86159, Germany

ARTICLE INFO

Keywords:
EBC
SiC/SiC CMC
Burner rig
Steam corrosion
Ytterbium silicate

ABSTRACT

Environmental Barrier Coating systems (EBCs) were thermally cycled in a burner rig test facility. $Yb_2Si_2O_7$ (YbDS) layer was deposited by air plasma spraying while two suspension plasma sprayed Yb_2SiO_5 (YbMS) microstructures were evaluated in duplex (YbDS/YbMS) systems: columnar and segmentation cracked. EBCs underwent 2000 cycles at a surface temperature of 1300 °C without signs of delamination failure. A porous YbMS layer formed at the base of intercolumnar gaps and segmentation cracks in the duplex systems, presumably due to reactions with entrapped water vapor. Furthermore, Yb_2O_3 depletion zones were evident at both the surface and YbDS/YbMS interface of the duplex EBCs.

1. Introduction

Plasma-sprayed thermal and environmental barrier coating systems (TBCs and EBCs) are used to protect structural components in the hot sections of gas turbine engines [1,2]. TBCs generally provide thermal insulation for metallic parts e.g. made of Ni-based superalloys while EBCs are applied on Si-based ceramics to protect against water vapor attack. The intrinsic porosity in these TBC topcoats serves to reduce the thermal conductivity [3,4] in the ceramic coating (7YSZ) as well as the in-plane coating modulus [5–7]. The latter is critical for imparting longevity under thermal cycling conditions, as there is a significant thermal expansion coefficient (CTE) mismatch between the metallic substrate (~14 ppm/K) and the ceramic coating (~10 ppm/K) [8]. EBCs, on the other hand, are intended to be (nearly) fully dense (ideally gas-tight) to hinder water vapor permeation through the thickness of the coating. This is necessary because water vapor can accelerate oxidation of the Si-based ceramic (e.g. Silicon Carbide, SiC), as water vapor can more easily diffuse into the material compared to oxygen [9]. In addition, the thermally-grown SiO_2 scale will volatilize with the water vapor, leading to the formation of $Si(OH)_4$ (g), and exposing unoxidized material [10]. CTE mismatch strains in an EBC system are not as critical when a $Yb_2Si_2O_7$ (YbDS) topcoat is used to protect the SiC, as both are in the range of 4–5 ppm/K [11]. However, in these water vapor environments, YbDS is also susceptible to steam corrosion [12–14] and will transform into Yb_2SiO_5 (YbMS) by Reaction (1).

$$Yb_2Si_2O_7 + 2H_2O\ (g) \rightarrow Yb_2SiO_5 + Si(OH)_4\ (g) \quad (1)$$

As mentioned, plasma spraying is one of the more conventional methods for TBC/EBC coating deposition on engine components. The process involves melting and accelerating solid powder particles (10–60 μm) toward a substrate. It is well-established so far that plasma spraying of YbDS particles will result in a composite coating consisting of YbDS+YbMS phases. This is due to the evaporation of SiO species from the YbDS particles during melting. It has been shown in past studies that depending on the particle temperatures achieved during the process, the YbMS concentration in the composite coating will vary; i.e. the hotter the particles, the higher the amount of YbMS [15–17].

Thermodynamic measurements of silica activity in the Yb_2O_3-SiO_2 system (which directly correlates with the reactivity of the system with water vapor) have been reported in both the Yb_2O_3-YbMS and YbMS-YbDS biphasic regions. These measurements revealed the silica activity in the Yb_2O_3-YbMS region to be two orders of magnitude lower than the YbMS-YbDS region, which implies better thermochemical stability of the former [18]. This result also agrees well with the known YbDS to YbMS transformation (Reaction 1) found in steam tests. Furthermore, other experimental works have shown that YbMS yields no measurable

* Corresponding author.
E-mail address: e.bakan@fz-juelich.de (E. Bakan).

https://doi.org/10.1016/j.corsci.2024.112174
Received 6 February 2024; Received in revised form 27 May 2024; Accepted 1 June 2024
Available online 3 June 2024

weight changes under the same test conditions as YbDS, which shows linear or parabolic mass loss kinetics depending on the test rig (i.e., depending on H_2O partial pressure, gas velocity, etc.) [19,20]. Therefore, using YbMS instead of YbDS as a protective layer against steam is a compelling option. However, the integration of YbMS in a Si/SiC system is also challenging due to the larger CTE of YbMS (7.2 ppm/K) [21] – which would result in larger thermal stresses during thermal cycling, especially under thermal gradient conditions. Moreover, YbMS shows high CTE anisotropy relative to crystallographic orientation [22], which adds further complexities if there are preferred orientations in the YbMS coatings after deposition.

In this work, the volatilization barrier, utilizing YbMS was investigated under representative thermal gradient (and water vapor) testing conditions as a potential environmental barrier coating for gas turbine application. Burner rig test which simulates high temperature and thermal gradients similar to those found in a gas turbine was used for this purpose. Based on the aforementioned available literature, having a YbMS top layer face the highest gas temperatures, velocities, and impinging water vapor is expected to be ideal. On the other hand, the presence of a through-thickness thermal gradient will inflate the CTE mismatch stresses in this system (especially in comparison with traditional isothermal testing conditions). Therefore, the YbMS layer was deposited as either columnar structured or segmentation cracked using the suspension plasma spray (SPS) process (Fig. 1). These microstructural features consequentially impart in-plane compliance which inherently reduces the sustained stresses in the YbMS [23–25]. However, as the intercolumnar gaps or segmentation cracks in the YbMS would provide fast diffusion paths for the oxidants, a dense, lamellar-structured YbDS layer was air plasma sprayed (APS) prior to the YbMS layers to serve as a secondary volatilization barrier. For comparative purposes, a single-layer YbDS system was also produced using APS process. The thickness of all the coatings (single layer and duplex) was kept to be around 200 μm. In the duplex coatings, the APS YbDS and SPS YbMS layers each were maintained at a thickness of ~100 μm. Similarly, the Si bond coat had a thickness of about 100 μm. All three EBC systems were then thermally cycled in a burner rig test facility at the surface temperatures of 1300–1400 °C for a constant 2000 cycles. While no coating delamination was observed, an unexpected reaction in the duplex coatings was found wherein free Yb_2O_3 in the YbMS coatings could react with surrounding $Si(OH)_4$ gases to form new YbMS.

2. Materials and methods

The Si bond coat and YbDS layers were air plasma sprayed on sintered α-SiC Hexoloy™ substrates (Saint Gobain Ceramics, Niagara Falls, NY) as well as on SiC/SiC CMC substrates (manufacturing details of the SiC/SiC material are available elsewhere [26]) both with a thickness of ~3 mm. The sintered Hexoloy substrates were used for microstructural evaluation and the CMC substrates were used for the burner rig testing. The YbDS and Si coatings were manufactured using a MultiCoat plasma spray controller (Oerlikon Metco, Wohlen, Switzerland) with a three-cathode TriplexPro 210 cascaded arc spray torch mounted on a six-axis robot (IRB 2400, ABB, Switzerland). APS process parameters and particle size information of commercial Si and YbDS feedstock (Oerlikon Metco, Wohlen, Switzerland) are summarized in Table 1.

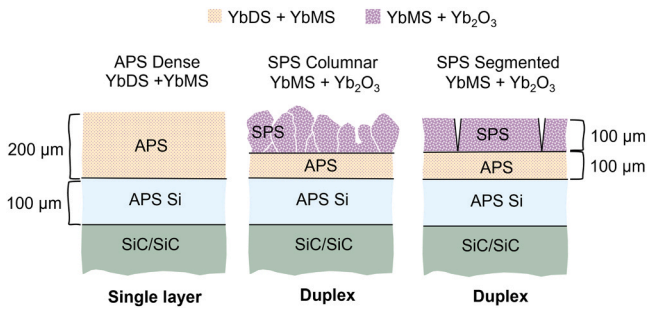

Fig. 1. Schematic of investigated EBC layer systems in this study.

After APS, the YbDS/Si-coated SiC substrates were coated again using suspension plasma spraying to deposit the YbMS layers. SPS topcoats were sprayed with an Axial III plasma torch (Northwest Mettech Corporation, Vancouver, Canada). The suspension was axially injected and a suspension feeding system developed by Forschungszentrum Jülich was used in this work [27]. SPS process parameters and information on the homemade ethanol-based suspensions are summarized in Table 2. The YbDS suspension was prepared by ball milling the same feedstock used in the APS process in ethanol. Further details of the preparation were described elsewhere [28]. YDS (d_{50}=33.9 μm, Treibacher Industrie AG, Althofen, Austria) and YbMS powders (d_{50}= 34.9 μm, Oerlikon Metco, Wohlen, Switzerland) were used for the preparation of YDS and YbMS suspensions, respectively. The particle size distribution of the suspensions was determined with the HORIBA LB-550 nanoparticle size analyzer (Retsch Technology GmbH, Haan, Germany). The feedstock size distributions to create columnar versus segmented SPS microstructures were chosen based on the literature [29]. Since even finer particles were required to achieve columnar microstructures, the feedstock chemistry was chosen to be a disilicate instead of directly a monosilicate, in an attempt to compensate for the expected feedstock decomposition during spraying. To screen the process parameter influence on microstructure, some pre-trials were conducted utilizing a YDS suspension instead of YbDS to reduce costs. Nevertheless, all burner-rig-tested coatings were YbDS/YbMS duplex EBCs. This is also indicated in Table 2.

Heat treatments of the produced layers were performed in a box furnace (1300 °C, 10 h) with a heating/cooling rate of 10 K/min. Each of the three EBC systems was then thermally cycled in a burner rig test facility where natural gas mixed with oxygen was combusted with simultaneous liquid water (1 g/min) injection. While the coated surface of the sample was heated by the combustion flame (5 min), the backside of the sample was impingement-cooled by compressed air at the same time, inducing a thermal gradient through the thickness of the sample. After this heating cycle, both sides of the sample were impingement-cooled down to room temperature by compressed air (2 min). The back and front side temperatures were monitored by infrared pyrometry (details are described in a former work [30]), the front surface temperatures were 1300 °C or 1400 °C while the backside temperatures were measured as 700–800 °C. Each sample was cycled 2000 times under these conditions.

Metallographic cross-sections of the as-sprayed and thermally-cycled coatings were prepared for microstructural investigations via scanning electron microscopy (SEM) using either a ZEISS EVO15 (Carl Zeiss Inc., United Kingdom), equipped with an Energy Dispersive Spectroscopy (EDS) detection system, [Oxford UltiMax100, Oxford Instruments, United Kingdom] or a ZEISS ULTRA 55 (Carl Zeiss NTS GmbH, Oberkochen, Germany) equipped with an EDS detection system [Octane Puls, EDAX, Ametek GmbH, Meerbusch, Germany]. Cross-sectional viewing and EDS analysis were carried out at 8 or 20 kV accelerating voltage in the backscatter mode. Additionally, confocal laser microscopy (Keyence VK-9700, Keyence, Osaka, Japan) was used. X-ray diffraction (XRD) was performed using a Bruker D4 Endeavor diffractometer (Bruker AXS GmbH, Karlsruhe, Germany) in Bragg-Brentano geometry using a Cu Kα radiation. Quantitative phase analysis of XRD patterns was carried out with the use of TOPAS V4 Software (Bruker AXS GmbH, Karlsruhe, Germany). The Vickers hardness measurement on as-sprayed and heat-treated YbDS surface was performed using a hardness tester (Duramin A300 Struers, Ballerup, Denmark).

Table 1
Air plasma spray parameters and feedstock particle size used for Si bond coat and YbDS topcoat deposition in this study.

Coating	Powder particle size	Current [A]	Power [kW]	Ar [slpm]	He [slpm]	Standoff distance (SOD) [mm]	Robot-velocity [mm/s]	Nozzle diameter [mm]
Si	(d_{10}=23.2, d_{50}=38.3, d_{90}=57.0 μm)	450	41	50	-	100	500	6.5
YbDS	(d_{10}=15.2, d_{50}=27.2, d_{90}=42.0 μm)	325	27.1	46	4	90	500	9

Table 2
Suspension plasma spray parameters and suspension information for columnar and segmentation cracked coatings produced in this study. Note that YDS suspension was only used for preliminary experiments for process optimization, and columnar SPS coatings for burner rig test samples were all produced from YbDS suspension.

Microstructure type	Suspension solid load and particle size	Current [A]	Voltage [V]	Power [kW]	Ar [slpm]	H_2 [slpm]	N_2 [slpm]	Standoff distance (SOD) [mm]	Robot-velocity [mm/s]	Cooling
Columnar	5 wt% YDS or YbDS + ethanol (d_{10}=0.1, d_{50}=0.5, d_{90}=2.2 μm)	660	140	92.4	183.8	36.8	24.5	70–90 (varied)	500	No cooling
Segmentation Cracked	10 wt% YbMS + ethanol (d_{10}=0.3,d_{50}=1.9, d_{90}=6.5 μm)	660	140	92.4	183.8	36.8	24.5	70	500	No cooling

3. Results and discussion

3.1. Microstructure of coatings

Fig. 2a-d shows cross-sectional microstructures of the SPS pre-trial coatings from Table 2 (YMS columnar (SOD 90 mm), YbMS segmentation cracked). Here, the influence of the crystallinity of the APS YbDS layer before SPS deposition was unclear. Therefore, the SPS coatings were sprayed on both as-sprayed (a, c) and heat treated (b, d) APS YbDS coatings. In all cases, a final post-SPS heat treatment was required to ensure full crystallinity of the duplex coatings. The microstructures of these coatings after the post-SPS heat treatment are shown in Fig. 2 a1-d1. The different material combinations and SPS microstructures are intentionally shown here to demonstrate a challenge that was observed in spraying SPS Yb/Y silicate layers on APS Yb-silicate layers, which was also dependent on the APS Yb-silicate crystallinity.

It can be seen in Fig. 2a, c that when either SPS layer was sprayed onto amorphous YbDS, the vertical cracks from both SPS layers propagated into the underlying APS layers and bifurcated. In a multi-layer system where the substrate is much thicker than the coating layers, coating layers with higher CTE than the substrate (e.g. monosilicate layers with CTE ~7 ppm/K) will be in tension during cooling from the deposition temperature (~700 °C) and are therefore susceptible to vertical cracking [31]. The bifurcation of the propagating cracks as they enter the YbDS layer implies a compressive stress state within the YbDS. Similar findings were reported in the literature for YbMS/mullite/Si [32] and HfO_2/YbDS/Si systems (i.e., high CTE / low CTE systems) [33]. It is important to note, however, that these coating systems were sprayed in a furnace (held at 1200 °C). Consequentially the coatings in these studies were highly dense and fully crystalline. Therefore it is difficult to directly compare the stress states of the coatings and adhesion properties of the interfaces in these aforementioned studies to this work.

Nonetheless, the cracks formed in the APS YbDS layers due to the SPS deposition were found to heal somewhat after the post-SPS heat treatment (Fig. 2 a1, c1). The governing mechanisms of this crack-healing phenomenon were discussed in detail elsewhere (in brief, a

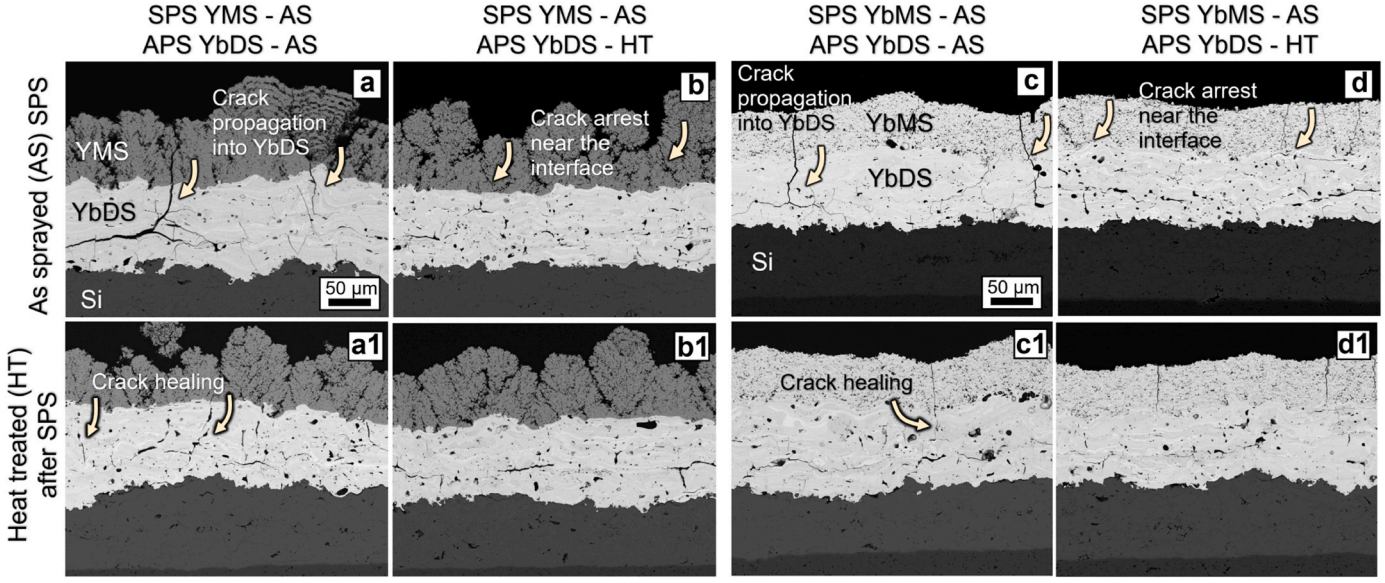

Fig. 2. Cross-section microstructures of as-sprayed SPS pre-trial coatings on as-sprayed (AS, a, c) and heat-treated (HT, b, d) APS YbDS layer. a1-d1 shows the microstructures of the same coatings after a heat treatment following the SPS process.

combination of viscous flow, solid-state sintering and metastable to stable phase transformations all contribute to the effects seen [34,35]). Interestingly, the crack propagation from the SPS into the APS layer could be circumvented in the first place when the SPS layers were directly sprayed onto fully crystalline YbDS layers (in other words, when the APS YbDS was annealed prior to SPS deposition) (Fig. 2b, d). As the SPS spraying conditions during spraying on amorphous and crystalline YbDS remained identical, i.e., same layer thickness/deposition rate, same coating chemical composition, same deposition temperature, etc., it can be argued that a similar amount of strain energy was released during the cooling phase (notwithstanding partial differences in the thermoelastic response of amorphous and crystalline solids). Assuming the sustained strain energies are similar, it is therefore surprising that the propagation of cracks from the SPS layer appear to have arrested at the APS/SPS interface.

From these first results, a difference in the fracture toughness of amorphous vs. crystalline YbDS layers was anticipated. Directly measuring the toughness or elastic properties of an amorphous glassy ceramic is incredibly challenging. However, in order to compare the toughness at least qualitatively, a Vickers hardness test was performed on the polished top surfaces (parallel to the substrate/coating interface) of the amorphous and crystalline YbDS coatings using 1 N test force. Fig. 3a-b shows the comparison of indentation-induced cracking on both of these surfaces at room temperature. The results clearly demonstrated an easier crack propagation on the as-sprayed/amorphous coating (Fig. 3a). These qualitative and comparative results can also help to explain the seemingly easier crack propagation tendency into amorphous YbDS after suspension plasma spraying of Yb/YMS layers.

Considering the presence of vertical cracks in the YbDS layer would inevitably shorten the lifetime of the EBC system due to accelerated attack by ingressing water vapor, the pre-trial results allowed us to conclude that all SPS layers to be thermally cycled in this work should be deposited on heat-treated/crystalline YbDS coatings. Nevertheless, some process optimizations were still necessary to avoid further delamination problems at the APS YbDS/SPS YbMS interface. As an example of these optimizations, the SPS YbMS microstructure sprayed on crystalline YbDS at a shorter standoff distance (70 vs. 90 mm) is shown in Fig. 4. To understand the propensity for delamination at 70 mm standoff, the effect of spraying the YbMS coating at closer standoff distances should be considered. First, the 70 mm standoff deposition resulted in a higher deposition temperature; additionally, the Yb_2O_3 content was lower (25 wt% at 70 mm standoff vs. 40 wt% at 90 mm standoff measured by XRD), likely due to a shorter time of flight of the particles in the plasma. Furthermore, the 70 mm standoff coating yielded a lower porosity, and inevitably a higher E-modulus. From the results in Fig. 4a and Fig. 4b, it is surmisable there was a higher stress/driving force for fracture at the 70 mm standoff distance. However, this cannot be a contribution of the Yb_2O_3 content because the bulk E modulus of YbMS and Yb_2O_3 are 172 [15] and 180 GPa [36], respectively, therefore E-modulus of the coating

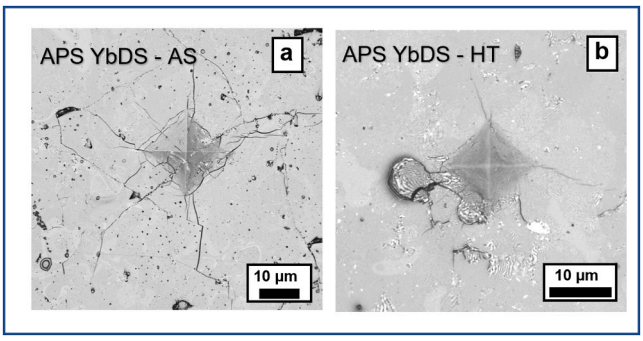

Fig. 3. Confocal laser microscope images of indentation-induced cracks at the surface of as-sprayed (AS) amorphous (a) and heat-treated (HT) crystalline (b) APS YbDS coatings under 1 N force.

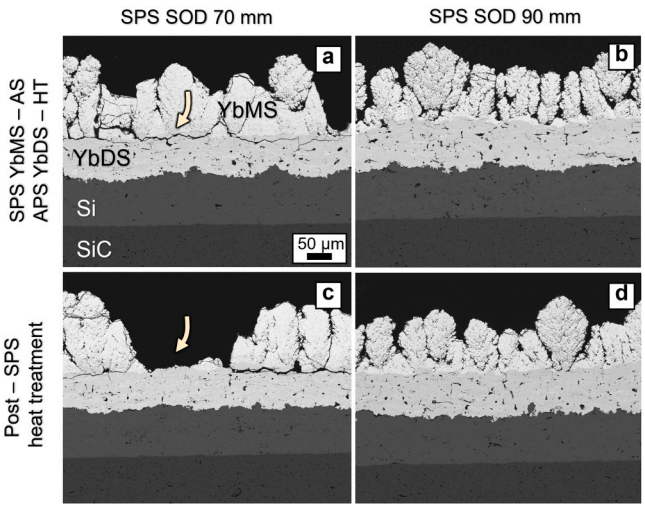

Fig. 4. Cross-section microstructures of as-sprayed SPS YbMS coatings deposited at 70 mm (a) and 90 mm (b) standoff distance on crystalline YbDS layers. c, d show the microstructures of the same coatings after a heat treatment following the SPS process. The arrows mark delamination cracks in the as-sprayed state (a) and a partially-delaminated area in the SPS layer after the heat treatment (c).

is not substantially affected by Yb_2O_3/YbMS ratio. Moreover, there should also be, a similar CTE mismatch due to the comparable CTE of YbMS (7.25 ppm/K, 100–1200 °C [22]) and Yb_2O_3 (6.8–8.4 ppm/K, 100–1200 °C [37]). Therefore, the source of the higher stress/driving force for coating fracture comes mainly due to the higher deposition temperature and higher E-modulus of the coating at the shorter standoff distance; these higher cooling stresses ($\sigma_{cooling}$) can be estimated according to [38];

$$\sigma_{cooling} = -\frac{E_c}{1-\nu}(\alpha_s - \alpha_c)\Delta T \quad (2)$$

where E_c is the E-modulus of the coating, ν is the Poisson ratio, α is the CTE of the substrate (s) and coating (c) and ΔT is the difference between deposition temperature and room temperature. As strain energy release rate for delamination (G_D) varies with the square of the stresses $\left(G_D = \frac{\sigma^2 h}{2E}\right)$ [39], a higher driving force for delamination can be anticipated at the shorter standoff distance (with higher deposition stresses) as observed by the experimental result. For that reason, the 90 mm standoff distance was chosen as the optimal condition to produce a columnar YbMS structure for thermal cycling tests.

3.2. Burner rig test results of single-layer APS YbDS

Water vapor is a byproduct of natural gas and oxygen combustion during burner rig testing, the impingement of which leads to volatilization of YbDS according to Reaction (1). Due to the radial thermal gradient within the sample during testing (i.e., edges are colder than the center of the disk sample) the volatilization rate will invariably be different along the surface, resulting in different YbMS scale thicknesses across the sample. More details on the spatially resolved phase composition of a similar sample after burner rig testing can be found in a previous publication [30]. Similarly, an increasing YbMS scale thickness from the edge towards the center of the sample was observed in this work after burner rig testing of the APS YbDS coating as presented in Fig. 5(a-c). Here, the conditions were kept at an average 1400 °C surface temperature and $T_{backside}$≈700 °C. For comparison, Fig. 5d shows a second APS YbDS sample which was tested at 1300 °C. The comparison of Fig. 5c-d reveals about 4 times larger (≈20 µm vs. 5 µm) YbMS

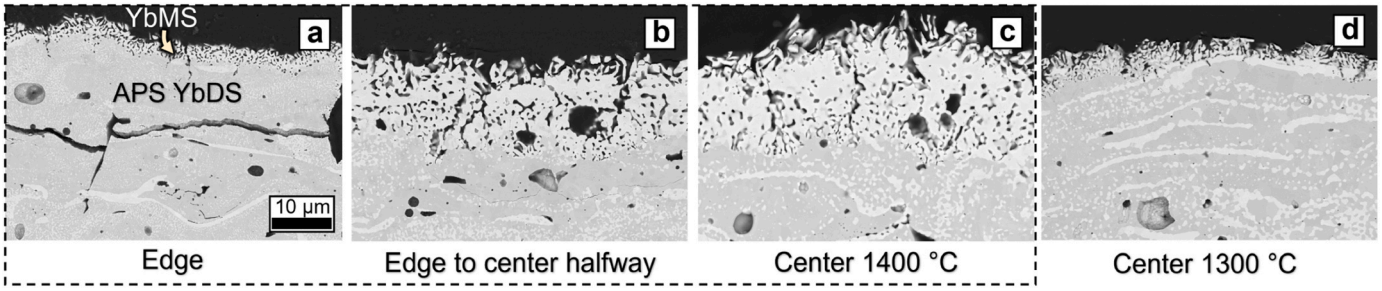

Fig. 5. Cross-section SEM images of thermally cycled (2000 cycles) APS YbDS layers at the top surface cycled at an average surface temperature of ~1400 °C (a-c), and 1300 °C (d) at the burner rig. The SEM images shown in a-b-c are taken from the same sample moving from the edge towards the center, respectively. The image d shows the center of an equivalent sample cycled at 1300 °C. Note that surface temperature is measured from the center of the sample by pyrometry during testing.

thickness with a 100 K increase in testing temperature. Additionally, the porosity in the YbMS layer appears to be lowest at 1400 °C at the center position, which may be a result of more enhanced sintering as the temperature reaches about 72 % of the melting point of YbMS.

Fig. 6 shows the entire cross-section of the APS YbDS sample after 2000 cycles of testing ($T_{surface}$=1300 °C) at the burner rig. The presence of cracks perpendicular to the coating surface propagating toward the CMC substrate indicated that the coating surface had been subjected to a large in-plane tensile stress during the testing [40]. It should be mentioned that the same type of cracking was also observed after testing at the 1400 °C surface temperature. Mud-cracking under thermal cycling in a temperature gradient is a known mechanistic response for TBCs. Limarga et al. attributed this phenomenon to the transient cooling period during burner rig testing [41]. Accordingly, by the end of the 5 min hold at the high temperature, any stresses in the coating are relaxed by creep deformation, particularly near the top surface relative to the interface with the metallic bond coat. Once the burner flame is removed from the surface, within the first few seconds, the coating surface temperature will abruptly drop down nearly to the substrate temperature due to the front impingement cooling [41]. This differential contraction through the thickness of the coating (as well as with the metal substrate) leads to tensile in-plane stresses at the coating surface, resulting in the mud cracking. During subsequent cooling, the larger CTE of the thick metallic substrate dictates the stress state, resulting in compressive stresses in the TBC. In the case of EBC systems, it can be assumed that a similar series of events should occur. Creep relaxation should take place at the high-temperature hold, and in-plane tensile stresses at the coating surface should form due to differential contraction during transient cooling. Thus the mud-cracking in the EBC system seen in Fig. 6 can be explained. For the SiC/Si/YbDS EBC system, the CTEs are much more similar, which implies two key points: first, the (relatively) large compressive stresses that form in the TBC/superalloy system upon cooling are not present here. Second, the magnitude of any stresses that form are significantly lower in the EBC system. Without these compressive stresses, any surface mudcrack formation is free to continue to propagate, which might explain why cracking through the silicon bond coat and CMC substrate was observed. When incorporating YbMS into the EBC system, larger (tensile) stresses can be assumed to develop at the same cycling conditions, which will be discussed next.

3.3. Burner rig test results of APS YbDS/SPS YbMS systems

While it was demonstrated in the previous section that higher-temperature cycling can be achieved in the burner rig which yielded accelerated volatilization rates, there were significant challenges in being able to sustain this surface temperature throughout the test. In some instances, the temperatures fluctuated to the point where melting of the underlying silicon bond coat was observed. It should be also mentioned that the emissivity of all coatings was assumed to be 1, which led to an underestimation of temperatures. These resulted in poor reproducibility in the high-temperature testing and, as a result, subsequent tests were constrained to the 1300 °C conditions.

Fig. 7(a, a1, b, b1) shows the cross-section of the columnar and segmented SPS YbMS on APS YbDS/Si coatings in the center of the sample after 2000 cycles of burner rig testing. In both samples, no delamination was observed after the tests. That said, the segmentation crack opening displacement was observed to be larger after burner rig testing (Fig. 7b vs. 7c). This is consistent with the previous discussion on transient cooling-induced tensile stresses, which can further open existing segmentation cracks. Furthermore, the wider crack opening

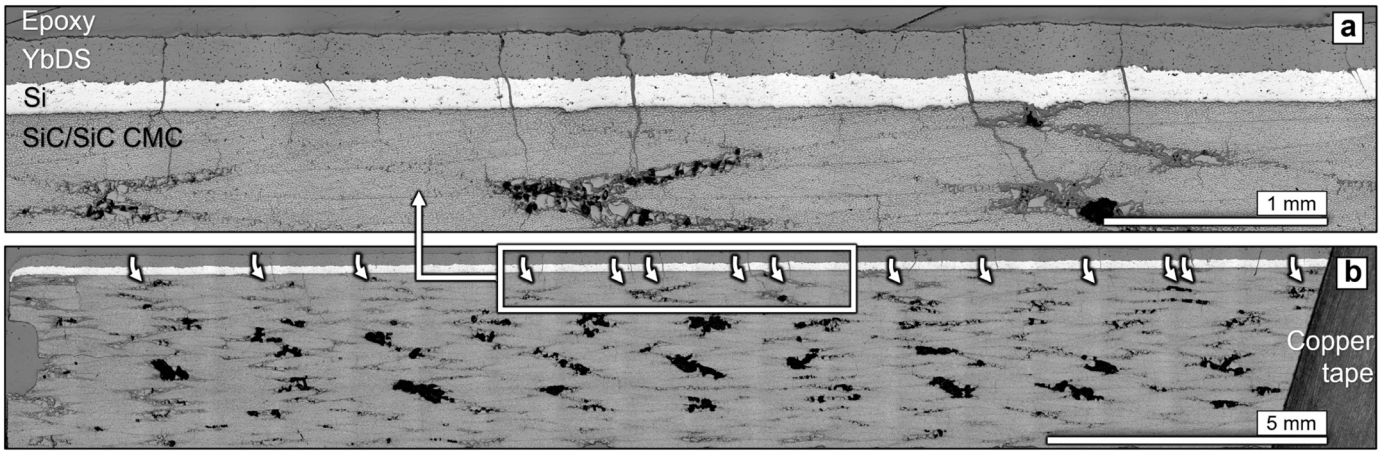

Fig. 6. Laser microscope images of SiC/SiC CMC/Si/YbDS system after 2000 cycles in the burner rig ($T_{surface}$=1300 °C). Arrows in the bottom image mark the position of mud cracks.

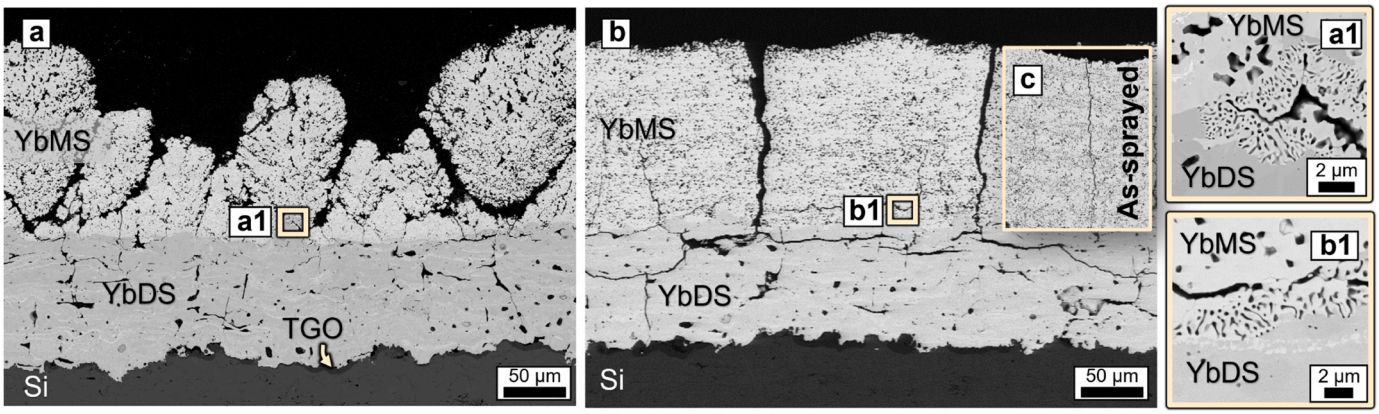

Fig. 7. SEM microstructures of columnar (a, a1) and segmented (b, b1) SPS YbMS on APS YbDS/Si coated CMC substrates after 2000 cycles of burner rig testing at 1300 °C surface temperature. As sprayed microstructure of the segmented coating is shown in c to demonstrate the increase in crack opening displacement after cycling.

displacement can be attributed to the effect of sintering in the SPS coating microstructure and the concomitant increase in the stiffness of the layer(s). Moreover, a higher energy release rate due to the increased stiffness can explain crack propagation in the underlying YbDS layer with the segmented SPS system. The bifurcation observed can be considered a direct consequence of the compressive stress states at the YbMS/YbDS interface due to the inherent CTE mismatch during cooling [33]. At prolonged cycling times, the linkage of such bifurcated cracks could ultimately lead to delamination of the YbMS layer and consequentially shorten the lifetime of the coating. In this regard, the columnar microstructure appears to provide enhanced durability as no crack propagation/bifurcation in the YbDS layer was observed. This could possibly be due to the higher strain tolerance of the columnar structure (higher density of vertical cracks = intercolumnar gaps in comparison with the segmented coating, see Fig. 7) over the course of cycling. These cracking events can be observed from the lower magnification images of the same samples shown in Fig. 8a-b. In contrast to single-layer APS YbDS, none of the duplex SPS/APS systems revealed vertical cracks running through the Si bond coat and CMC substrate after burner rig testing (Fig. 6 vs. Fig. 8). In this regard, both columnar and segmented YbMS microstructures compared to the near-fully dense APS YbDS are proven to be advantageous, likely owing to the higher strain tolerance. This becomes more clear when considering the fact that all systems underwent similar transient cooling conditions leading to potentially larger tensile stresses forming during cooling in the YbMS layers. Furthermore, CTE-driven compression in the YbDS layer under the YbMS layer in the duplex APS/SPS system may be beneficial to fight against the propagation of through-thickness mudcracks into the substrate.

In both columnar and segmented SPS systems, at the YbDS/YbMS interface, where the columnar gaps or segmentation cracks terminate, a porous YbMS region was found (Fig. 7 a1-b1) suggesting the water vapor reaction (Reaction 1) took place here as well. It is important to note in the case where the cracks bifurcated, water vapor reactions were observed within the YbDS at the bifurcation crack termination points. The thickness of these 'embedded reaction zones' was found to be about 2 μm, which is nearly half of the YbMS layer thickness measured at the surface of the single-layer APS YbDS coating at the same region of the sample (Fig. 5d). The difference in reaction layer thicknesses can be associated with the lower gas impingement velocities and temperature in these embedded regions by comparison with the coating surface, which could reduce the rate of SiO_2 volatility/reactivity.

Table 3 summarizes the phase compositional changes of SPS samples quantitatively before and after the burner rig testing. As the SPS coatings were amorphous in the as-sprayed state, exact phase compositions could only be properly determined after a heat treatment. Accordingly, the columnar SPS coating which was produced from a YbDS suspension contained 60/40 wt% YbMS/Yb_2O_3 before the burner rig test, which suggests significant SiO_2 loss during spraying from submicron particles (as anticipated). The segmented coating on the other hand had 89/11 wt

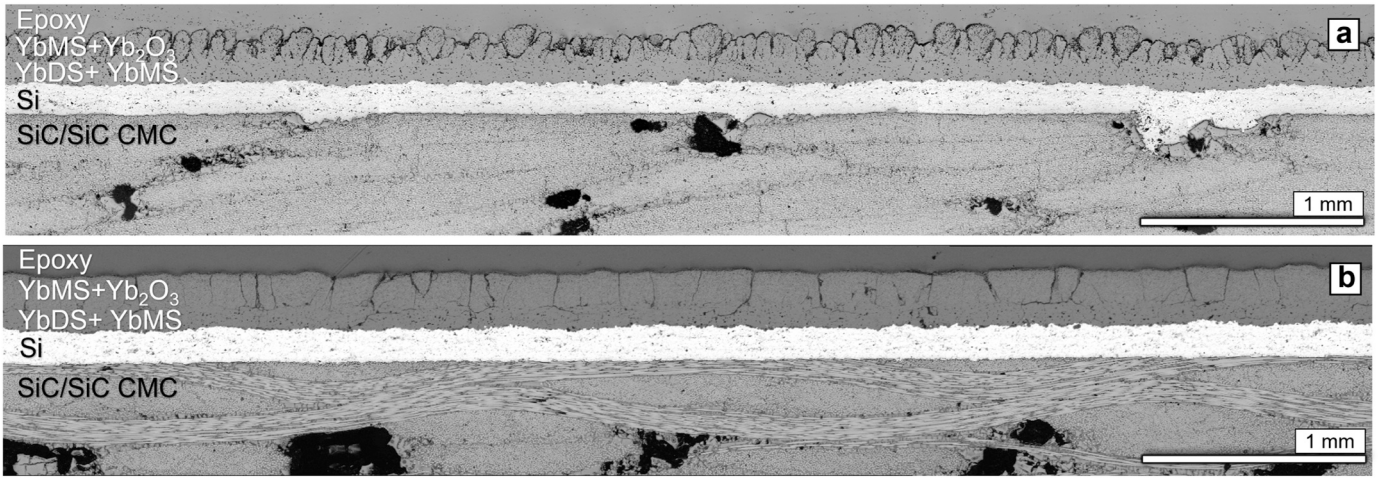

Fig. 8. Laser microscope images of columnar (a) and segmented (b) SPS YbMS on APS YbDS/Si coated CMC substrates after 2000 cycles of burner rig testing at 1300°C surface temperature. The images taken from the central part of the sample are stitched as shown for the single-layer APS YbDS coating in Fig. 6a.

Table 3
Rietveld analysis results of the XRD data measured from the SPS coatings (measurements were taken from the center of the samples) before (after a crystallization heat treatment) and after the burner rig test (2000 cycles, $T_{surface}$=1300 °C). X-ray diffractograms can be seen in the supplementary file, S1.

Microstructure	Phase composition after heat treatment, before burner rig test		Phase composition after burner rig test	
	Yb_2SiO_5 (YbMS, wt%)	Yb_2O_3 (wt%)	Yb_2SiO_5 (YbMS, wt%)	Yb_2O_3 (wt%)
Columnar SPS	60	40	78	22
Segmented SPS	89	11	98	2

% YbMS/Yb_2O_3 ratio before the burner rig test. After testing, the YbMS content in both coatings (which can be considered to be near the top surface, as the X-rays only penetrate some tens of microns into the surface) increased, while conversely the Yb_2O_3 amounts were seen to be decreasing. This increase in YbMS/decrease in Yb_2O_3 could be also confirmed using SEM and EDS analyses, as shown in Fig. 9 for the segmented coating as an example. Fig. 9a shows the cross-sectional microstructure of the coating near the top surface where three different regions can clearly be identified; a very porous outer reaction layer (3), a dense intermediate layer (2), and a porous, unreacted inner region (1). Regions 2–3 are single-phase based on the BSE contrast while region (1) consists of two different phases. According to EDS maps shown in Fig. 9 b1-b3, the phase with the lighter contrast, which is also marked with an arrow in the maps, is Yb_2O_3 and the matrix phase with the darker contrast is YbMS. This result agrees well with the 98/2 wt% YbMS/YbO_2 content measured with XRD from the same coating after burner rig test.

3.4. *Proposed interactions between silicate EBCs and gas burner rig flames*

Based on the existing literature, YbMS is expected to show superior water vapor corrosion resistance than YbDS due to its lower silica activity; it reacts with water vapor to form $Si(OH)_4$ by Reaction (2) [42,43].

$$Yb_2SiO_5 + 2H_2O\ (g) \rightarrow Yb_2O_3 + Si(OH)_4\ (g) \quad (3)$$

Therefore, it is logical to expect an increase in Yb_2O_3 content as the amount of YbMS decreases during burner rig testing. However, the results of this work showed an opposite trend. No Yb_2O_3 layer was observed at the surface of YbMS coatings after burner rig testing, neither in cross-sectional analysis (Fig. 9) nor by surface XRD analysis (Table 3), despite the anticipated transformation according to Reaction (2). A similar result was also reported by Wang et al. in the literature [44]. The authors here explained their findings by assuming a higher steam volatilization rate of Yb_2O_3 in comparison with the YbMS, referring to the study of Courcot et al., which examined analogous yttrium silicates [45]. Courcot et al. suggested that above 1320 °C, SiO_2 is more stable than Y_2O_3 under a moist environment. The authors estimated through thermodynamic calculations the vapor pressure of $Y(OH)_3$ gas over the corresponding oxide to be ~10^{-6} bar at 1600 K in a 'moist environment' (n_{Ar} = 0.4 mol, n_{O2}=0.1 mol, n_{H2O} = 0.5 mol). Parker and Opila however showed that Y_2O_3 is highly stable compared to SiO_2 under the same steam testing conditions [42]. A more recent study by Bauschlicher et al. using a DFT modeling approach yielded roughly the same vapor pressure of $Y(OH)_3$ (~10^{-6} bar) at 1600 K. Moreover, this work has shown the vapor pressure of $Yb(OH)_3$ over Yb_2O_3 to be even smaller than the yttrium hydroxides, at 10^{-10} bar at 1600 K (50 % H_2O/Ar), thereby implying ytterbia has even higher stability in moist environments compared to SiO_2 [46]. Furthermore there are other studies suggesting that $Si(OH)_4$ has a much higher vapor pressure than the rare-earth hydroxides [18,47,48].

Based on the conclusions drawn from these studies, a hypothesis toward the unexpected results in this work can be formed. If it is assumed that the Yb_2O_3 present in the YbMS coating is stable in the burner rig test because of the significantly lower vapor pressure of $Yb(OH)_3$ compared to $Si(OH)_4$ (forming from the simultaneous volatilization of YbMS), then there must be an abundance of $Si(OH)_4$. Therefore, a more likely mechanistic hypothesis is that free Yb_2O_3 in the coating reacted with outwardly-diffusing $Si(OH)_4$ (produced by Reaction 1 or 2) and transformed to YbMS during burner rig testing.

As a basis for this hypothesis, Y_2O_3 was shown to react with a trace amount of $Si(OH)_4$ (g) to form YMS at elevated temperatures in the literature, e.g. the $Si(OH)_4$ formed by the steam corrosion of SiC tube (sample holder) or quartz capillary of the steam test setup was enough to form YMS on Y_2O_3 samples by Reaction (3) [42,49].

$$Y2O3 + Si(OH)4\ (g) \rightarrow Y2SiO5 + 2H2O(g) \Delta G^{o}_{rxn,\ 1450°C} = -317.70 kJ/mol \quad (4)$$

It should be mentioned that unlike the aforementioned works, in the burner rig test environment, the only source of $Si(OH)_4$ (g) can be produced by Reaction (1 or 2).

In the literature, after steam jet furnace testing of YbDS [50] and YDS [42] (1300–1400 °C, 200 m/s gas velocity, P_{H2O}=1 atm), a dense intermediate (Yb, Y)MS layer between the porous (Yb, Y)MS and porous (Yb, Y)$_2O_3$ layers was observed. The authors attributed the dense YbMS formation on porous YbMS to Reaction (3), i.e. $Si(OH)_4$ diffusing outward from the interface which experiences Reaction (2), the diffusing Si $(OH)_4$ can then react with the Yb_2O_3 that has already formed at the porous YbMS surface. Densification in the newly formed YbMS layer was attributed to the volume expansion due to the $Si(OH)_4$ uptake by Yb_2O_3 and its propensity to sinter at elevated temperatures. One caveat to consider is the water vapor partial pressure and gas velocities reached in the aforementioned steam test are expected to be significantly higher in comparison with the burner rig used in this work [42,50] which may explain the continuous (Yb, Y)$_2O_3$ layer formation according to Reaction (2) in the former. In this work, however, the YbMS coating already inherently has free Yb_2O_3 phase after SPS processing as mentioned above. It should also considered that the reaction constant of reaction (2) is extremely small, i.e. it will run from right to left if sufficient Si $(OH)_4$ is supplied. Only in the vicinity of a fast flowing gas flow in which $Si(OH)_4$ is removed efficiently establishing very low pressures, Yb_2O_3 will be formed.

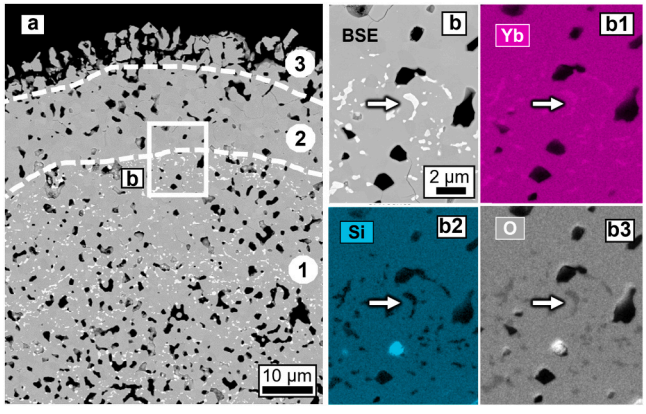

Fig. 9. Back-scattered electron (BSE) SEM image of the segmented SPS YbMS coating (center of the sample) after the burner rig test (a). Image (b) shows the higher magnification BSE-SEM image taken from the region marked with the rectangle in the image (a). Yb (b1), Si (b2), O (b3) EDS maps of the image (b). Dashed lines in (a) indicate the notional boundaries of regions numbered from 1 to 3, and arrows in b, b1, b2, and b3 mark the same particle in each image and serve as a guide to the eye.

Another important distinction between the burner rig test and isothermal furnace tests is the presence of thermal gradients – both through-thickness and radially across the specimen surface in the former. Fig. 10 demonstrates the effect of the radial and through-thickness temperature gradient on the segmented coating after burner rig testing. Microstructural coarsening due to more enhanced sintering can be easily observed at the center of the sample (Fig. 10b) when compared to the edge (Fig. 10a), where the temperature is expected to be lower. Similarly, in the through-thickness direction, densification near the surface of the YbMS coating, particularly at the centermost location, was more evident in comparison with the region close to the YbDS/YbMS interface (Fig. 10b). As mentioned earlier, conversion of Yb_2O_3 to YbMS by $Si(OH)_4$ uptake via Reaction (3) might be contributing to the densification near the top surface. However, Reaction 3 is also seen to take place deeper into the duplex coating, at the YbDS/YbMS interface; yet there is evidently less pronounced densification at this location (Fig. 10b2). The water vapor reactions at this region are further discussed below. Nevertheless, the results suggest that densification near the topmost YbMS layer surface was likely sintering-driven due to high-temperature exposure. It is presumable that the densification near the surface could 'entrap' the $Si(OH)_4$ gaseous species that form within the coating system, thereby leading to $Si(OH)_4$ partial pressure buildup within the coating while water vapor partial pressure at this same location decreases due to the topmost densification. In this event, the reaction quotient (for Reaction (3), $Q=(P_{H2O})^2/(P_{Si(OH)4})$ could get smaller than 1 and contribute to a negative non-standard Gibbs free energy ($\Delta G=\Delta G^{\circ}+RTln[Q]$, where ΔG° is standard Gibbs free energy, R is ideal gas constant and T is temperature [51]) and thus produce conditions for a thermodynamically favorable reaction.

The $Si(OH)_4$ (g) source resulting in the Yb_2O_3 depletion near the YbDS/YbMS interface (Fig.10b2) is presumed to be Reaction (1). As shown above, in Fig. 7b1, the distinct porous structure forms at the base of the YbMS segmentation cracks (similar porous structures at the YbDS/YbMS interface can be also seen in Fig. 10 b, b2 at the base of segmentation cracks). The presence of this porous phase serves as a qualitative indicator that Reaction (1) probably took place in this region. Therefore, it can be assumed that burner rig testing, especially of duplex multicomponent EBCs with through-thickness segmentation cracks, can generate unique environmental conditions – such that a tertiary reaction induced by the $Si(OH)_4$ (g) that forms due to the known volatilization of rare earth silicates with water vapor can consume any free rare earth oxide (Yb_2O_3) within the system to form new monosilicate (YbMS) material. It should be mentioned that the same phenomenon was also observed in the columnar system. That said, possibly due to higher Yb_2O_3 content in this system (40 wt% vs. 11 wt%, Table 3) before testing, the depletion was less noticeable in the columnar system after testing (see image comparison S2 in the supplementary file).

4. Summary

A burner rig thermal gradient test facility with a natural gas + oxygen combustion source and simultaneous water injection into the burner flame was used to study the thermal cycling performance, thermochemical stability and microstructural evolution of three unique EBC systems (single layer dense APS YbDS+YbMS (i), duplex layered columnar SPS YbMS+Yb_2O_3/ dense APS YbDS+YbMS (ii), and duplex layered segmented SPS YbMS+Yb_2O_3/ dense APS YbDS+YbMS (iii). The tests were carried out for a constant 2000 cycles and performed at surface temperatures ranging from 1300 to 1400 °C, while the specimen backside temperatures were kept within a 700–800 °C range.

No delamination failure was observed after the burner rig tests in any of the EBC systems. After testing, through-thickness mud cracks were observed in the dense single-layer YbDS + YbMS coating, propagating into the CMC substrate, which was attributed to the tensile stress state formed by transient cooling in burner rig testing. In the SPS systems, no such cracks were found, presumably due to higher in-plane compliance of columnar/segmented SPS microstructures. However, in the duplex system with segmentation cracks, these cracks were found to penetrate and bifurcate into the underlying YbDS layer – likely due to the compressive stress state due to CTE mismatch strains between YbMS and YbDS. In prolonged thermomechanical testing, the bridging of these bifurcated cracks may drive delamination failure. Beyond the thermomechanical findings, several thermochemical interactions were observed in this work. Fig. 11 summarizes the thermochemical changes found in the tested systems after burner rig testing. As the chemical changes were similar for the columnar and segmented-cracked SPS coatings, only the segmented coating is illustrated in the figure (Fig. 11b-c). In agreement with previous studies on this material, a porous YbMS layer formed at the surface of the APS single-layer YbDS coating according to Reaction (1) (Fig. 11a). Surprisingly, similar porous

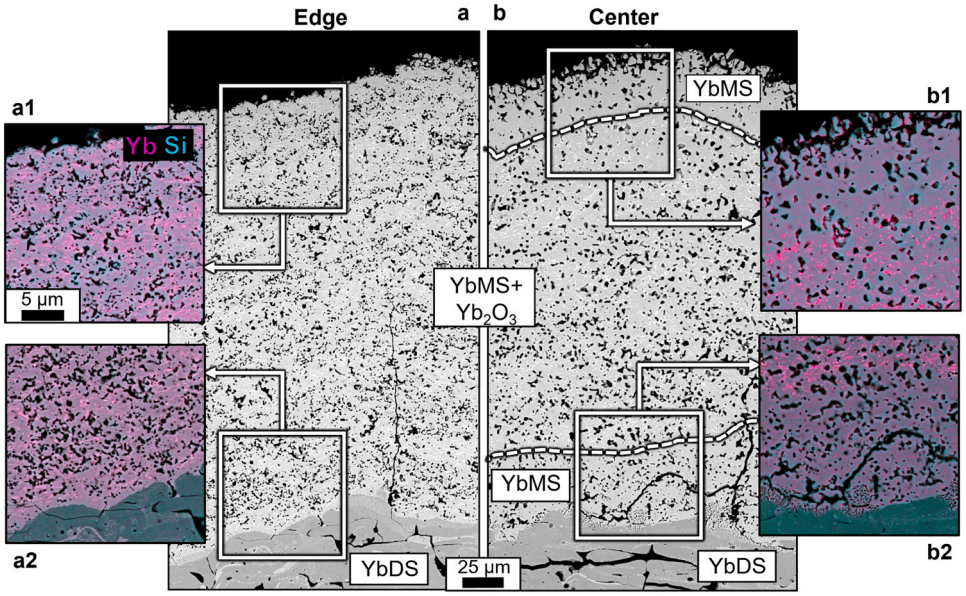

Fig. 10. BSE-SEM images of segmented SPS coating taken from the edge (a) and center (b) of the burner rig sample. Overlapped Yb, Si EDS maps (a1, a2, b1, b2) measured from the marked areas in a and b.

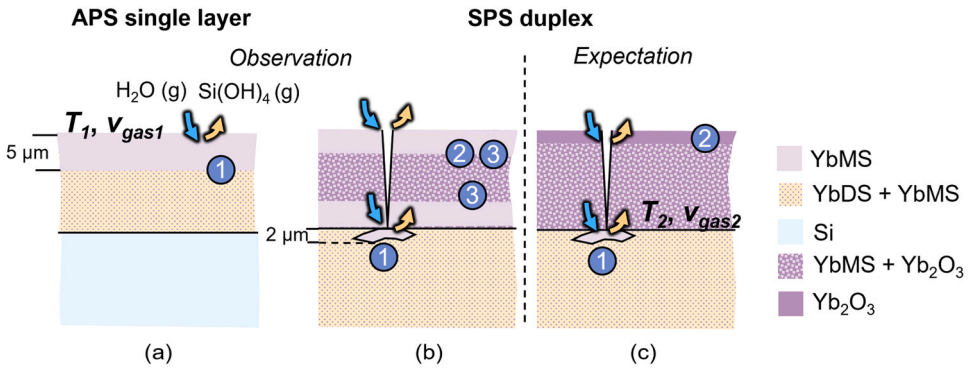

Fig. 11. Summary of thermochemical changes observed after burner rig testing for the single layer APS YbDS + YbMS (a) and duplex segmentation cracked SPS YbMS + Yb_2O_3/ APS YbDS + YbMS (b) EBC systems. Image (c) depicts the expected chemical change in the duplex layered system based on the literature. 1–3 indicates the reaction numbers that are given throughout the manuscript.

reacted structures were also observed at the interfaces of the APS/SPS duplex systems, notably at the bottom of intercolumnar gaps or segmentation cracks (Fig. 11b). The thickness of these interfacial porous reaction zones was about 2 µm, which was nearly half of the thickness of the surface YbMS layer that grew on the single-layer APS YbDS + YbMS coating (≈ 5 µm). This difference was attributed to higher gas temperature and velocity at the coating surface (T_1, v_{gas1}) compared to the interface (T_2, v_{gas2}). As shown in Fig. 11c, an enrichment in the Yb_2O_3 concentration at the surface of the SPS coatings was expected according to Reaction (2) and assuming higher stability of Yb_2O_3 in steam compared to $Si(OH)_4$-forming YbMS. Instead, a depletion in the Yb_2O_3 content was found both near the surface of the YbMS + Yb_2O_3 coating and at the APS YbDS/SPS YbMS interface (Fig. 11b). As a first hypothesis, free Yb_2O_3 depletion was explained by Reaction (3), wherein the Si $(OH)_4$ (g) (produced by Reaction (2) at the surface, and Reaction (1) at the interface) is consumed. Future work will attempt to prove this hypothesis.

Author statement

The authors declare that the science contained in this manuscript has not been previously published and is not under consideration by any other journal.

CRediT authorship contribution statement

Emine Bakan: Conceptualization, Investigation, Writing - Original draft, Writing - Review & Editing, Visualization. **Dapeng Zhou**: Investigation. **Daniel E. Mack**: Investigation. **Dietmar Koch**: Resources. **Robert Vaßen**: Supervision.

Declaration of Competing Interest

The authors declare that they have no known competing financial interests or personal relationships that could have appeared to influence the work reported in this paper.

Data availability

The data that has been used is confidential.

Acknowledgements

The authors are grateful to Frank Kurze for thermal spray assistance and Dr. Doris Sebold for SEM/EDS assistance. Special thanks to Dr. Edward Gildersleeve for fruitful discussions and help with SEM/EDS analyses.

Appendix A. Supporting information

Supplementary data associated with this article can be found in the online version at doi:10.1016/j.corsci.2024.112174.

References

[1] D.R. Clarke, M. Oechsner, N.P. Padture, Thermal-barrier coatings for more efficient gas-turbine engines, MRS Bull. 37 (10) (2012) 891–898.
[2] K.N. Lee, Enviromental Barrier Coatings For SiC/SiC, in: N.P. Bansal, J. Lamon (Eds.), in *Ceramic Matrix Composites: Materials, Modeling and Technology*, The American Ceramic Society, 2015.
[3] K.W. Schlichting, N.P. Padture, P.G. Klemens, Thermal conductivity of dense and porous yttria-stabilized zirconia, J. Mater. Sci. 36 (12) (2001) 3003–3010.
[4] T.W. Clyne, et al., Porous materials for thermal management under extreme conditions, Philos. Trans. R. Soc. A: Math., Phys. Eng. Sci. 364 (1838) (2006) 125–146.
[5] B. Siebert, et al., Changes in porosity and Young's modulus due to sintering of plasma sprayed thermal barrier coatings, J. Mater. Process. Technol. 92-93 (1999) 217–223.
[6] T. Nakamura, G. Qian, C.C. Berndt, Effects of pores on mechanical properties of plasma-sprayed ceramic coatings, J. Am. Ceram. Soc. 83 (3) (2000) 578–584.
[7] J.A. Thompson, T.W. Clyne, The effect of heat treatment on the stiffness of zirconia top coats in plasma-sprayed TBCs, Acta Mater. 49 (9) (2001) 1565–1575.
[8] P.K. Wright, A.G. Evans, Mechanisms governing the performance of thermal barrier coatings, Curr. Opin. Solid State Mater. Sci. 4 (3) (1999) 255–265.
[9] B.E. Deal, A.S. Grove, General relationship for the thermal oxidation of silicon, J. Appl. Phys. 36 (12) (1965) 3770–3778.
[10] E.J. Opila, Oxidation and volatilization of silica formers in water vapor, J. Am. Ceram. Soc. 86 (8) (2003) 1238–1248.
[11] H. Chen, et al., Hydrothermal synthesis of ytterbium silicate nanoparticles, Inorg. Chem. 49 (4) (2010) 1942–1946.
[12] N. Maier, K.G. Nickel, G. Rixecker, High temperature water vapour corrosion of rare earth disilicates (Y,Yb,Lu)2Si2O7 in the presence of Al(OH)3 impurities, J. Eur. Ceram. Soc. 27 (7) (2007) 2705–2713.
[13] S. Ueno, et al., Comparison of water vapor corrosion behaviors of Ln2Si2O7 (Ln=Yb and Lu) and ASiO4 (A=Ti, Zr and Hf) EBC's, Key Eng. Mater. 317-318 (2006) 557–560.
[14] Fritsch, M., PhD Thesis, Heißgaskorrosion keramischer Werkstoffe in H2O-haltigen Rauchgasatmosphären, in Fakultät Maschinenwesen. 2007, Technische Universität Dresden: Germany.
[15] B.T. Richards, H.N.G. Wadley, Plasma spray deposition of tri-layer environmental barrier coatings, J. Eur. Ceram. Soc. 34 (12) (2014) 3069–3083.
[16] E. Bakan, et al., Effect of processing on high-velocity water vapor recession behavior of Yb-silicate environmental barrier coatings, J. Eur. Ceram. Soc. 39 (4) (2019) 1507–1513.
[17] R. Vaßen, et al., Correlation of process conditions, porosity levels and crystallinity in atmospherically plasma sprayed Yb2Si2O7 environmental barrier coatings, J. Compos. Sci. 5 (8) (2021) 198.
[18] G.C.C. Costa, N.S. Jacobson, Mass spectrometric measurements of the silica activity in the Yb2O3–SiO2 system and implications to assess the degradation of silicate-based coatings in combustion environments, J. Eur. Ceram. Soc. 35 (15) (2015) 4259–4267.
[19] K.N. Lee, D.S. Fox, N.P. Bansal, *Rare earth silicate environmental barrier coatings for SiC/SiC composites and Si_3N_4 ceramics.* J. Eur. Ceram. Soc. 25 (10) (2005) 1705–1715.
[20] H. Klemm, Silicon nitride for high-temperature applications, J. Am. Ceram. Soc. 93 (6) (2010) 1501–1522.
[21] Z. Tian, et al., Theoretical and experimental determination of the major thermo-mechanical properties of RE2SiO5 (RE = Tb, Dy, Ho, Er, Tm, Yb, Lu, and Y) for

environmental and thermal barrier coating applications, J. Eur. Ceram. Soc. 36 (1) (2016) 189–202.
[22] M. Ridley, et al., Tailoring thermal properties of multi-component rare earth monosilicates, Acta Mater. 195 (2020) 698–707.
[23] M. Ahrens, et al., Sintering and creep processes in plasma-sprayed thermal barrier coatings, J. Therm. Spray. Technol. 13 (3) (2004) 432–442.
[24] B. Lv, et al., Sintering resistance of advanced plasma-sprayed thermal barrier coatings with strain-tolerant microstructures, J. Eur. Ceram. Soc. 38 (15) (2018) 5092–5100.
[25] S.V. Shinde, et al., Segmentation crack formation dynamics during air plasma spraying of zirconia, Acta Mater. 183 (2020) 196–206.
[26] B. Mainzer, et al., Development of polyvinylsilazane-derived ceramic matrix composites based on Tyranno SA3 fibers, J. Ceram. Soc. Jpn. 124 (10) (2016) 1035–1041.
[27] A. Guignard, et al., Deposition and characteristics of submicrometer-structured thermal barrier coatings by suspension plasma spraying, J. Therm. Spray. Technol. 21 (3) (2012) 416–424.
[28] D. Zhou, et al., Sintering behavior of columnar thermal barrier coatings deposited by axial suspension plasma spraying (SPS), J. Eur. Ceram. Soc. 39 (2) (2019) 482–490.
[29] K. VanEvery, et al., Column Formation in Suspension Plasma-Sprayed Coatings and Resultant Thermal Properties, J. Therm. Spray. Technol. 20 (4) (2011) 817–828.
[30] E. Bakan, et al., An investigation on burner rig testing of environmental barrier coatings for aerospace applications, J. Eur. Ceram. Soc. 40 (15) (2020) 6236–6240.
[31] M.R. Begley, J.W. Hutchinson, The Mechanics and Reliability of Films, Multilayers and Coatings, Cambridge University Press, Cambridge, 2017.
[32] B.T. Richards, M.R. Begley, H.N.G. Wadley, Mechanisms of ytterbium monosilicate/mullite/silicon coating failure during thermal cycling in water vapor, J. Am. Ceram. Soc. 98 (12) (2015) 4066–4075.
[33] J.A. Deijkers, M.R. Begley, H.N.G. Wadley, Failure mechanisms in model thermal and environmental barrier coating systems, J. Eur. Ceram. Soc. 42 (12) (2022) 5129–5144.
[34] E. Bakan, R. Vaßen, Crack healing mechanisms in atmospheric plasma sprayed Yb-silicate coatings during post-process heat treatment, J. Eur. Ceram. Soc. 43 (8) (2023) 3684–3693.
[35] E. Bakan, Y.J. Sohn, R. Vaßen, Metastable to stable phase transformation in atmospheric plasma sprayed Yb-silicate coating during post-heat treatment, Scr. Mater. 225 (2023) 115169.
[36] B.R. POWELL JR, O. HUNTER JR., W.R. Manning, Elastic properties of polycrystalline ytterbium oxide, J. Am. Ceram. Soc. 54 (10) (1971) 488–490.
[37] S. Stecura, W.J. Campbell, U.S. department of the interior, bureau of mines, Therm. Expans. Phase Invers. Rare-earth Oxides (1961).
[38] S. Kuroda, T.W. Clyne, The quenching stress in thermally sprayed coatings, Thin Solid Films 200 (1) (1991) 49–66.
[39] T.W. Clyne, S.C. Gill, Residual stresses in thermal spray coatings and their effect on interfacial adhesion: a review of recent work, J. Therm. Spray. Technol. 5 (4) (1996) 401.
[40] A.G. Evans, J.W. Hutchinson, The mechanics of coating delamination in thermal gradients, Surf. Coat. Technol. 201 (18) (2007) 7905–7916.
[41] A.M. Limarga, R. Vaßen, D.R. Clarke, Stress distributions in plasma-sprayed thermal barrier coatings under thermal cycling in a temperature gradient, J. Appl. Mech. 78 (1) (2010) 011003. -011003-9.
[42] C.G. Parker, E.J. Opila, Stability of the Y2O3–SiO2 system in high-temperature, high-velocity water vapor, J. Am. Ceram. Soc. 103 (4) (2020) 2715–2726.
[43] R.A. Golden, E.J. Opila, A method for assessing the volatility of oxides in high-temperature high-velocity water vapor, J. Eur. Ceram. Soc. 36 (5) (2016) 1135–1147.
[44] Y. Wang, et al., Water vapor corrosion behaviors of plasma sprayed ytterbium silicate coatings, Ceram. Int. 46 (18, Part A) (2020) 28237–28243.
[45] E. Courcot, et al., Thermochemical stability of the Y2O3–SiO2 system, J. Eur. Ceram. Soc. 30 (4) (2010) 905–910.
[46] C.W. Bauschlicher Jr., N.S. Jacobson, Thermochemistry of gaseous ytterbium and gadolinium hydroxides and oxyhydroxides, J. Phys. Chem. A 125 (14) (2021) 2913–2922.
[47] E.J. Opila, D.S. Fox, N.S. Jacobson, Mass spectrometric identification of Si–O–H(g) species from the reaction of silica with water vapor at atmospheric pressure, J. Am. Ceram. Soc. 80 (4) (1997) 1009–1012.
[48] N.S. Jacobson, Silica activity measurements in the Y2O3–SiO2 system and applications to modeling of coating volatility, J. Am. Ceram. Soc. 97 (6) (2014) 1959–1965.
[49] M. Fritsch, et al., Corrosion of selected ceramic materials in hot gas environment, J. Eur. Ceram. Soc. 26 (16) (2006) 3557–3565.
[50] M. Ridley, E. Opila, Thermochemical stability and microstructural evolution of Yb2Si2O7 in high-velocity high-temperature water vapor, J. Eur. Ceram. Soc. (2020).
[51] O. Kubaschewski, C.B. Alcock, P.J. Spencer, Materials Thermochemistry, Pergamon Press, 1993.